

# 1 **Turbulent erosion of a subducting intrusion in the Western** 2 **Mediterranean Sea**

3 Giovanni Testa<sup>1</sup>, Mathieu Dever<sup>2,3</sup>, Mara Freilich<sup>4</sup>, Amala Mahadevan<sup>2</sup>, T. M. Shaun Johnston<sup>5</sup>, Lorenzo  
4 Pasculli<sup>1,6</sup>, Francesco M. Falcieri<sup>1</sup>

5 <sup>1</sup> Institute of Marine Sciences, Italian National Research Council (CNR-ISMAR), Venice, Italy.

6 <sup>2</sup> Woods Hole Oceanographic Institution, Woods Hole, 02543, MA, USA

7 <sup>3</sup> RBR, Ottawa, Canada

8 <sup>4</sup> Brown University, Providence, RI, USA

9 <sup>5</sup> Scripps Institution of Oceanography, University of California, San Diego, La Jolla, CA, USA

10 <sup>6</sup> Department of Environmental Sciences, Informatics and Statistics, University Ca' Foscari of Venice, Via Torino 155, 30172  
11 Mestre, Italy

12 *Correspondence to:* Giovanni Testa (giovanni.testa@ve.ismar.cnr.it)

13 **Abstract.** Frontal zones within the Western Alboran Gyre (WAG) are characterized by a density gradient resulting from the  
14 convergence of Atlantic and Mediterranean waters. Subduction along isopycnals at the WAG periphery can play a crucial role  
15 in upper ocean ventilation and influences its stratification and biogeochemical cycles. In 2019, physical parameters  
16 (comprising temperature, salinity, turbulent kinetic energy dissipation rates) and biogeochemical data (oxygen and  
17 chlorophyll-a) profiles were collected in transects along the northern edge of the WAG. Several intrusions of subducted water  
18 with elevated oxygen, chlorophyll-a and spice anomaly were identified towards the center of the anticyclone. These features  
19 had elevated kinetic energy dissipation rates on both their upper and lower boundaries. Analysis of the turbulent fluxes  
20 involving heat, salt, oxygen, and chlorophyll-a demonstrated a net flux of physical and biogeochemical properties from the  
21 intrusions to the surrounding ocean. Either the turbulent or diffusive convection mixing contributed to the observed dilution  
22 of the intrusion. Other factors (e.g., water column density stability, variability of the photic layer depth, and organic matter  
23 degradation) likely played a role in these dynamics. Enhanced comprehension of the persistence and extent of these features  
24 might lead to an improved quantitative parametrization of relevant physical and biogeochemical properties involved in  
25 subduction within the study zone.

## 26 **1 Introduction**

27 The Mediterranean Sea is characterized by a shallow circulation cell and a complex upper-layer circulation featuring numerous  
28 quasi-permanent eddies and fronts (Tanhua et al., 2013; Capó et al., 2019; Barral et al., 2021; Bonaduce et al., 2021;  
29 Zarokanellos et al., 2022; Sánchez-Garrido and Nadal, 2022). The main 12 Mediterranean thermal fronts were listed by Belkin  
30 and Cornillon (2007), whereas a recent work by Sudre et al. (2023) captured an even more complex scenario. Specifically,  
31 frontal zones in the Alboran Sea (Western Mediterranean basin) are characterized by a density gradient resulting from the

32 convergence of Atlantic and Mediterranean waters (Fedele et al., 2022; Garcia-Jove et al., 2022). The Atlantic jet strongly  
33 influences the formation of two large-scale anticyclonic gyres within the Alboran Sea (the Eastern and Western Alboran Gyres,  
34 WAG; **Fig. 1A**) with a smaller cyclonic gyre typically situated in between (Brett et al., 2020; Sala et al., 2022; Sánchez-Garrido  
35 and Nadal, 2022).

36 Ocean subduction, defined as the physical transfer of water from the mixed layer into the ocean interior (Williams,  
37 2001), plays a pivotal role in upper-ocean ventilation and stratification. It also exerts a profound influence on biogeochemical  
38 cycles, thereby contributing to the export of greenhouse gases and the vertical transport of organic carbon (Omand et al., 2015;  
39 Olita et al., 2017; Stukel et al., 2017; Ruiz et al., 2019; Zarokanellos et al., 2022). The vertical component of ocean current  
40 velocity is typically much smaller than its horizontal counterparts, but areas characterized by meandering frontal features  
41 associated with mesoscale eddies are expected to exhibit elevated subduction rates (van Haren et al., 2006). Indeed, vertical  
42 velocities of up to  $55 \text{ m d}^{-1}$  have been observed in the Western Alboran Sea front (Capó and McWilliams, 2022; Garcia-Jove  
43 et al., 2022; Rudnick et al., 2022), and net submesoscale subduction rate has been estimated at  $0.3 \text{ m day}^{-1}$  (Freilich and  
44 Mahadevan, 2021). Mesoscale turbulence contains more energy than submesoscale patterns (Storer et al., 2022), although  
45 submesoscale features can generate larger vertical velocities than mesoscale structures within frontal zones (Mahadevan, 2016;  
46 Ruiz et al., 2019). The relationship between submesoscale velocity and mixing within the boundary layer has been explored  
47 in prior studies under conditions of turbulent thermal wind balance (Crowe and Taylor, 2018; McWilliams, 2021) and  
48 symmetric instabilities (Thomas et al., 2013; Bachman et al., 2017; Zhou et al., 2022). However, so far there has been limited  
49 research that specifically identifies occurrences of quasi-balanced subsurface vertical velocity and examines how mixing  
50 responds to such instances.

51 Vertical motion at fronts is driven by frontogenesis, instability processes, nonlinear Ekman effects, and  
52 filamentogenesis (Klein and Lapeyre, 2009; Mahadevan, 2016; Mahadevan et al., 2020a; McWilliams, 2021; Capó and  
53 McWilliams, 2022; Garcia-Jove et al., 2022). Instabilities have also been identified as a key source of turbulence and energy  
54 dissipation at oceanic fronts (D'Asaro et al., 2011; Carpenter et al., 2020; McWilliams, 2021). Subsurface intrusions carry  
55 physical (temperature and salinity) and biogeochemical properties (oxygen and chlorophyll-a) characteristic of the surface  
56 mixed layer along isopycnals and extend downward and laterally. Intrusions are often identified because of the co-occurrence  
57 of subsurface maxima in oxygen, particulate organic carbon with anomalous temperature and salinity properties (i.e., spice;  
58 Omand et al., 2015). Intermittent intrusions subducting along the outer periphery of mesoscale and submesoscale structures  
59 have previously been identified (Johnston et al., 2011; Llorc et al., 2018; Chapman et al., 2020; Johnson and Omand, 2021;  
60 Chen et al., 2021; Capó and McWilliams, 2022; Freilich et al., 2024). This study measures the turbulent erosion of a subducting  
61 intrusion at fronts within the Western Alboran Gyre, a major mesoscale feature in the western Mediterranean Sea with a Rossby  
62 number of 0.08. Data were collected in the framework of the Coherent Lagrangian Pathways from the Surface Ocean to Interior  
63 (CALYPSO) project onboard the R/V *Pourquois Pas?*, that aimed to examine subduction features in close proximity to the  
64 unstable front that developed along the northern edge of the WAG (Mahadevan et al., 2020).

65 Previous studies have investigated turbulence data collected with microstructure probes in both the surface (Cuypers  
66 et al., 2012; Forryan et al., 2012; Vladoiu et al., 2021) and deep (Ferron et al., 2021; van Haren, 2023) regions of the Western  
67 Mediterranean Sea. However, this work represents the first comprehensive investigation of turbulence in a context of  
68 mesoscale-submesoscale subduction at frontal zones within the WAG. This paper begins with a comprehensive description of  
69 water column properties and a turbulence dataset. We then conduct an examination of physical and biogeochemical properties  
70 across frontal transects to identify and characterize subducting features. Finally, we calculate the turbulent erosion of a selected  
71 intrusion of interest.

## 72 **2 Material and methods**

### 73 **2.1 Sampling strategy and profile inventory**

74 The study zone is highly dynamic and significantly influenced by the eastward-flowing Atlantic jet that sustains the WAG  
75 (Sánchez-Garrido and Nadal, 2022). The jet is characterized by a pronounced frontal zone, exhibiting a density contrast of up  
76 to  $1.0 \text{ kg m}^{-3}$  at its boundaries (Oguz et al., 2014).

77 We conducted five transects across the salinity front identified through operational modeling and satellite estimations  
78 in the northern edge of the WAG between March 28<sup>th</sup> and April 4<sup>th</sup> 2019 (**Fig. 1B**). Temperature and salinity conditions in the  
79 upper water column were sampled with an Underway Conductivity Temperature Depth (UCTD) profiler, resulting in a total  
80 of 136 profiles (mean depth: 231 m). Turbulence data were collected on 43 stations (mean depth: 219 m) during the campaign  
81 using a microstructure profiler. With the exception of a single station, all stations featured duplicate microstructure profiles,  
82 from which the mean value between these replicates was computed. Furthermore, we used a CTD probe to obtain 22 dissolved  
83 oxygen and chlorophyll-a profiles (mean depth: 284 m) concurrently with the microstructure profiles.

### 84 **2.2. Temperature, salinity and derived variables**

85 Temperature and salinity data were acquired using a Teledyne RD Instruments UCTD profiler, as detailed by Rudnick and  
86 Klinke (2007). The sampling rate is 16 Hz, with the UCTD falling velocity ranging between 1.5 and 3.5  $\text{m s}^{-1}$ . The spatial  
87 resolution between UCTD cycles was approximately 1 km, given a cruise speed of 3  $\text{m s}^{-1}$  knots during recovery. The UCTD  
88 downcasts were post-processed for sensor alignment, salinity spikes correction and were binned using a spline interpolation  
89 onto a vertical grid of 1 m. A comprehensive description of data post-processing procedures can be found in Dever et al.,  
90 (2019). Key oceanographic parameters, including absolute salinity, conservative temperature, Brunt–Väisälä frequency ( $N^2$ ),  
91 density ratio and Turner angle and spice were computed using the Gibbs Sea Water oceanographic toolbox of TEOS-10  
92 (<https://www.teos-10.org/pubs/gsw>).

93  $N^2$  serves as an indicator of water column vertical stability and was determined using equation (1):

$$94 \quad N^2 = - \frac{g}{\rho_w} \frac{\partial \rho}{\partial z} \quad (1)$$

95 where  $g$  represents gravitational acceleration ( $9.8 \text{ ms}^{-2}$ ),  $\rho_w$  is a reference seawater density ( $1025 \text{ kg m}^{-3}$ ), and  $\partial\rho/\partial z$  denotes  
96 the variability of potential density with depth. The density ratio quantifies the vertical contributions of conservative  
97 temperature and absolute salinity to the stability of the water column (following the Thermodynamic Equation of Seawater –  
98 2010; IOC et al., 2010). The Turner angle, as outlined by McDougall et al., (1988), was computed to identify water column  
99 conditions, including double diffusivity (thermal diffusivity or salt fingering), stability, and instability regimes. Seawater spice,  
100 defined as the temperature and salinity variability along isopycnals, was employed to discern water masses with similar density,  
101 but varying temperature and salinity characteristics (McDougall et al., 2021). Spice anomaly was computed with respect to the  
102 mean spice profile computed in a temperature-salinity space (McDougall and Krzysik, 2015) and obtained including all spice  
103 profiles of the dataset. When computing the mean spice for a given density, we effectively combine specific temperature and  
104 salinity values that correspond to that density. The resulting spice anomaly then quantifies the deviation of the water parcel  
105 with the same density from the mean temperature-salinity combination, enabling the identification of intrusions. Furthermore,  
106 mixed layer depth was determined using a density threshold of  $0.03 \text{ kg m}^{-3}$  relative to the reference density at 10 m depth, as  
107 proposed by de Boyer Montégut et al. (2004). Isopycnal strain, which measures the stretching or compression of isopycnal  
108 surfaces, was calculated as the vertical gradient of isopycnal displacement (Pinkel et al., 1991). This displacement is defined  
109 as the difference between the actual depth of each isopycnal and its expected depth based on the mean density profile calculated  
110 along the entire section.

### 111 **2.3. Detection of subducting intrusions**

112 Observational evidence of water being subducted from the upper ocean layer to below the mixed layer was observed by  
113 leveraging the high spatio-temporal resolution of the underway data collected by the UCTD. The presence of subsurface  
114 intrusions in a frontal transect was semi-automatically detected from the vertical profiles, based on subsurface spice and  
115 temperature anomalies. The detection algorithm proceeds as follows: I) Compute average spice on isopycnals for the campaign  
116 (auto). II) Compute spice anomaly on an isopycnal for each profile phase (auto). III) Detect subsurface anomalies in spice  
117 anomaly using a peak-finding algorithm based on peak prominence (auto). IV) Retain anomalies with at least 5 samples (i.e.,  
118 1.5 m; auto) and occur coherently over more than 3 consecutive profiles (manual).

119

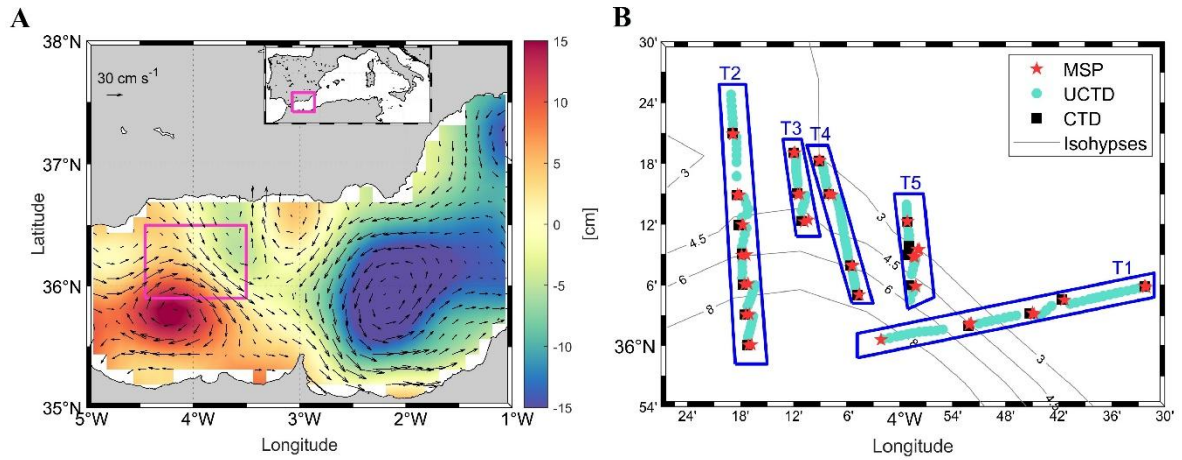


**Figure 1.** (A) Map of the Alboran Sea showing the mean absolute dynamic topography (colors) and geostrophic currents (arrows) on March 30<sup>th</sup>-31<sup>st</sup>, 2019. The purple inset shows the location of the sampling effort, detailed in panel (B), where blue rectangles denote the sampling stations selected for transect (T#) analysis. T1 was realized on March 29<sup>th</sup>, T2 on March 30<sup>th</sup> and T3-T5 on March 31<sup>st</sup>. Isohyps of absolute dynamic topography are depicted as gray lines. Red stars, cyan circles and black squares correspond to sampling stations for the microstructure profiler, underway CTD and CTD, respectively. Daily absolute dynamic topography and geostrophic current data were downloaded from <https://data.marine.copernicus.eu/>.

## 2.4. Dissolved oxygen and Chlorophyll-a

We equipped a SeaBird 911plus CTD probe with a SeaBird 43 dissolved oxygen sensor and a WET Labs ECO-AFL/FL fluorometer to assess dissolved oxygen and chlorophyll-a concentrations, respectively. The CTD data underwent bin-averaging to achieve a vertical resolution of 0.5 m and was subsequently calibrated using in situ data. Dissolved oxygen estimates were aligned with measurements obtained through Winkler titration ( $n = 67$ ; Mahadevan et al., 2020b), while chlorophyll-a estimates derived from fluorescence were calibrated against data from fluorometric determinations ( $n = 140$ ; Alou-Font et al., 2019). A high level of agreement was found between in situ measurements and CTD-derived estimations, as evidenced by coefficient of determination ( $R^2$ ) values of 0.99 for dissolved oxygen and 0.85 for chlorophyll-a.

Oxygen and chlorophyll-a anomaly on isopycnals were computed following equation (2):

$$X_a = X_p - \bar{X}_p \quad (2)$$

where  $X_a$  represents the variable (i.e., oxygen or chlorophyll-a) anomaly,  $X_p$  denotes the observed value at a specific density and  $\bar{X}_p$  is the mean property value corresponding to this density.

## 2.5. Horizontal ocean currents, Richardson number and potential vorticity

Horizontal current magnitude and direction were collected using a hull-mounted Teledyne RDI Ocean Surveyor Acoustic Doppler Current Profiler (ADCP) operating at a frequency of 150 kHz and with a vertical bin size of 4 m. Detailed post-processing procedures for ADCP data have been exhaustively documented in Mahadevan et al. (2020b) and Cutolo et al.

(2022). Shear squared ( $S^2$ ) was calculated from ADCP data as the sum of the squares of the vertical gradients of the horizontal velocity components (Gregg, 1989). This value was subsequently used to estimate the Richardson number for shear instabilities (expressed as the ratio between  $N^2$  and  $S^2$ ; Cushman-Roisin and Beckers, 2011). Ertel potential vorticity (PV) was calculated according to Zhmur et al. (2021) and equation (3):

$$PV = -(f + \zeta) \frac{\partial b}{\partial z} + \left( \frac{\partial v}{\partial z} \frac{\partial b}{\partial x} - \frac{\partial u}{\partial z} \frac{\partial b}{\partial y} \right) \quad (3)$$

where  $f$  is the Coriolis parameter,  $\zeta$  is the relative vorticity,  $\partial b/\partial z$  corresponds to the vertical buoyancy gradient,  $\partial b/\partial x$  and  $\partial b/\partial y$  are the horizontal buoyancy gradients, and  $u$  and  $v$  represent the horizontal current components.

## 2.6. Turbulent kinetic energy dissipation rates

Various methods have been employed to quantify turbulent mixing (e.g., integral approaches, finescale parameterizations and direct microstructure measurements; Thorpe, 2005; Shroyer et al., 2018). In this study, we present turbulence dissipation rates observations and derived parameters (Thorpe, 2005) collected using a free-falling microstructure profiler (MSS90D; Sea & Sun Technology). The probe was equipped with two microstructure shear sensors (PNS6), with the final turbulent dissipation rate calculated as the mean of the two shear probe estimates. The profiler's buoyancy was adjusted to achieve a sinking velocity between 0.6 and 0.7 m s<sup>-1</sup> and the data sampling occurred at a frequency of 1024 Hz but was internally averaged to 512 Hz to comply with signal degradation along the 1.2 km probe cable. Post-processing and turbulent dissipation rate calculations were carried out using the microstructure profiler processing toolbox developed by Schultz et al. (2022). We fine-tuned instrument-specific parameters according to the microstructure profiler employed in this study (e.g., sampling frequency, sensors calibration and sensitivity, distance of other sensors to the shear sensor's tip), while the threshold parameters for data validation from Schultz et al. (2022) were retained. These processing routines were evaluated using two benchmark ATOMIX (Analysing Ocean Turbulence Observations to Quantify Mixing) datasets (Fer et al., 2024), which adhere to best practices for estimating dissipation rates from shear probes (Lueck et al., 2024). The analysis showed strong consistency ( $R^2 = 0.98$ ) between ATOMIX data processed using the Schultz et al. (2022) routines and the Lueck et al. (2024) approach (**Supplementary Fig. 1**), with the former slightly overestimating dissipation rates by a mean of 1.6%.

Kinetic energy dissipation rates ( $\epsilon$ ) were computed as per equation (4):

$$\epsilon = 15\nu \overline{\left( \frac{\partial u}{\partial z} \right)^2} \quad (4)$$

where  $\nu$  represents the kinematic molecular viscosity and  $\overline{(\partial u/\partial z)^2}$  is the spatial average of vertical shear variation with depth (Taylor, 1935). Turbulent dissipation rates from both shear probes were treated separately, averaging all shear spectra within 1 m vertical bin. The shear spectrum results were iteratively fitted to the Nasmyth (Nasmyth, 1970) reference shear spectrum and the deviation of the observed spectrum with respect to the Nasmyth's was used for data quality check. A detailed description of the data processing procedure was described in Schultz et al. (2022). We performed data-averaging at 1-meter

174 depth intervals, excluding the initial 15 meters of each profile, to mitigate the noise arising from ship motion and wave-  
175 breaking (D'Asaro, 2014).

176 The microstructure data exhibited good agreement ( $R^2 = 0.89$ ) between the two shear sensors ( $n=8957$ ;  
177 **Supplementary Fig. 2A**), with a stronger correlation observed under elevated turbulence conditions ( $\varepsilon > 10^{-7} \text{ W kg}^{-1}$ ) compared  
178 to calmer waters ( $\varepsilon < 10^{-7} \text{ W kg}^{-1}$ ). Another quality control parameter was the magnitude of the pseudo dissipation rates  
179 originated from the profiler high frequency vibrations, consistently one order of magnitude lower than turbulent kinetic energy  
180 dissipation rates (**Supplementary Fig. 2B**) and predominantly (36.9%) falling within the range of  $1.0 \cdot 10^{-10}$  to  $1.6 \cdot 10^{-10} \text{ W kg}^{-1}$ .  
181 <sup>1</sup>.

## 182 2.7 Turbulent fluxes

183 Vertical diffusivity ( $K_z$ ) is computed according to equation (5):

$$184 K_z = \gamma \frac{\varepsilon}{N^2} \quad (5)$$

185 where the mixing efficiency is  $\gamma = 0.2$  (Gregg et al., 2018; Mouriño-Carballido et al., 2021; Lozovatsky et al., 2022),  $\varepsilon$  is the  
186 turbulent kinetic energy dissipation rate and  $N^2$  denotes the squared buoyancy frequency.

187 We determine turbulent heat (in units of  $\text{W m}^{-2}$ ) and salt fluxes ( $\text{kg m}^{-2} \text{ s}^{-1}$ ) following Sheehan et al. (2023) and  
188 equations (6) and (7):

$$189 Q_H = -\rho C_p K_z \frac{\partial \theta}{\partial z} \quad (6)$$

$$190 Q_S = 10^{-3} \left( -\rho K_z \frac{\partial S}{\partial z} \right) \quad (7)$$

191 where  $\rho$  is seawater density,  $C_p$  is the specific heat capacity of seawater ( $3850 \text{ J kg}^{-1} \text{ }^\circ\text{C}^{-1}$ ),  $\partial\theta/\partial z$  corresponds to the vertical  
192 gradient of conservative temperature, and  $\partial S/\partial z$  indicates the vertical gradient of absolute salinity. Furthermore, turbulent  
193 fluxes of dissolved oxygen and chlorophyll-a (in units of  $\text{mg m}^{-2} \text{ s}^{-1}$ ) were estimated using equations (8) proposed by Williams  
194 et al. (2013):

$$195 Q_X = -K_z \frac{\partial X}{\partial z} \quad (8)$$

196 where  $\partial X$  denote the variable (i.e., oxygen or chlorophyll-a) vertical gradient with depth.

197 Our analysis primarily focused on the subducting intrusion identified along transect 2 during the 2019 CALYPSO campaign  
198 (**Fig. 1B**). The limited number of microstructure profiles precluded a comprehensive analysis of spatiotemporal intrusions  
199 variability along the other transects. To assess the physical and biogeochemical conditions around the subducting intrusion  
200 boundaries, we calculated the mean conditions within 5 m inside and outside the intrusion boundaries. The methodology used  
201 to calculate diapycnal turbulent fluxes does not account for advective terms involving diapycnal velocity (Du et al., 2017) and  
202 assume a constant mixing efficiency ( $\gamma$ ) of 0.2. However,  $\gamma$  can vary depending on stratification, turbulence intensity, and water  
203 column regimes (Canuto et al., 2011; Gregg et al., 2018). Despite this, variability in  $\gamma$  is typically smaller compared to

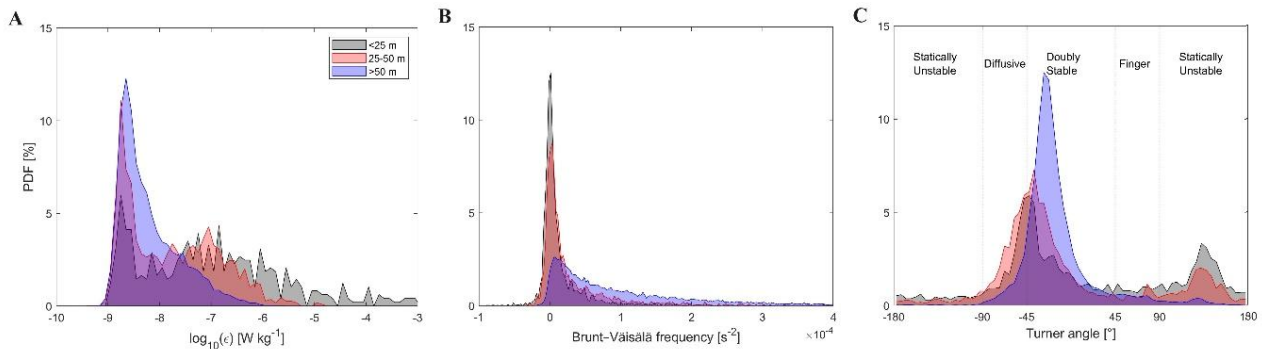
204 variations in turbulence (Le Boyer et al., 2023). It is important to note that the assumption of identical vertical diffusivity for  
 205 heat, salt, and tracers may introduce potential inaccuracies in flux estimates, which should be considered.

## 206 3 Results

### 207 3.1 Water column stability and turbulent kinetic energy dissipation rates

208 High mixing was observed in the surface layer, with localized turbulence peaks in the subsurface water column. Turbulent  
 209 kinetic energy (TKE) dissipation values displayed considerable variability, with 43.8% of observations falling between  $1.3 \cdot 10^{-9}$   
 210  $^9$  and  $4.0 \cdot 10^{-9} \text{ W kg}^{-1}$  (mean  $\pm$  standard deviation:  $8.2 \cdot 10^{-9} \pm 2.4 \cdot 10^{-8} \text{ W kg}^{-1}$ ), with a peak (11.2%) identified in the range of  
 211  $2.0 \cdot 10^{-9}$  to  $2.5 \cdot 10^{-9} \text{ W kg}^{-1}$ . An analysis of  $\epsilon$  probability distribution by depth intervals indicated that 95% of deep  $\epsilon$  values were  
 212 comprised between  $10^{-9}$  and  $10^{-7} \text{ W kg}^{-1}$  (**Fig. 2A**). In contrast, surface and mid-water depths exhibited a lower proportion  
 213 (53% and 77%, respectively) within this  $\epsilon$  range. Surface waters (<25 m) were characterized by elevated  $\epsilon$  values, with 25%  
 214 and 12% of the data falling within the ranges of  $10^{-7}$ - $10^{-6}$  and  $10^{-6}$ - $10^{-5} \text{ W kg}^{-1}$ , respectively.

215 Elevated homogeneity in the shallow water column vertical structure was observed. Indeed, the probability  
 216 distribution of Brunt–Väisälä frequency ( $N^2$ ) by depth intervals (**Fig. 2B**) indicated lower stratification in the surface and mid-  
 217 water layers, where approximately 81% and 67% of values were lower than  $0.2 \cdot 10^{-4} \text{ s}^{-2}$ , respectively. Conversely, the deeper  
 218 portion (>50 m) of the water column exhibited stronger stratification, with an increased proportion (70%) of  $N^2$  estimations  
 219 exceeding  $0.3 \cdot 10^{-4} \text{ s}^{-2}$ . These patterns were reflected in water column conditions. Examination of Turner angle values revealed  
 220 a predominantly stable water column, accounting for 74% of the dataset (**Fig. 2C**). However, these stability conditions  
 221 exhibited notable variations with depth. The shallow layer displayed a more varied scenario with a near-equal distribution  
 222 between statically unstable and doubly stable conditions. In contrast, the mid-water column featured the highest proportion  
 223 (27%) of diffusive regimes and the deep layer was primarily characterized (83%) by double stable conditions.



224  
 225 **Figure 2.** Probability distribution frequency (PDF) by depth intervals for turbulent kinetic energy dissipation rates (A), Brunt–Väisälä  
 226 frequency (B) and Turner angle values (C). Colored shaded areas in panels correspond to different depth intervals, with gray: 15-25 m; red:  
 227 26-50 m; blue: depths >51 m. The names in panel (C) reflect the water column regime according to the Turner angle value (McDougall et  
 228 al., 1988).



### 230 3.2 Transects across the Western Alboran Gyre front

231 A noticeable depression in the isopycnals was consistently observed in all the transects extending towards the interior of the  
 232 anticyclone (**Fig. 3** and **Supplementary Fig. 3-7**). The highest  $\varepsilon$  below the mixed layer was detected adjacent to zones featuring  
 233 elevated vertical density gradients and deepening along the isopycnals in transects 2 (**Fig. 3**). A deepening of positive spice  
 234 anomalies from approximately 50 to 100 m was observed at the start of transect 1 and from 15-35 km of transect 2. Subducting  
 235 intrusions were observed along all transects, except for transect 3, possibly owing to its shorter length (approximately 12 km;  
 236 **Fig. 3** and **Supplementary Fig. 3-7**). The mean thickness of subducting intrusions was computed at 14.2 m (standard deviation:  
 237 9.4 m), ranging from a minimum of 1.7 to a maximum of 42.2 m. The subduction is likely occurring along the frontal direction,  
 238 following the anticyclonic circulation, rather than necessarily along the tilted isopycnals identified in the transect.

239 Enhanced  $\varepsilon$  and diffusivity values were noted in proximity to the base of the mixed layer and in the vicinity of  
 240 subducting intrusion boundaries (**Fig. 4**). Furthermore, diffusive water column conditions were identified along the upper  
 241 boundary of the subducting intrusion in transect 2 (**Fig. 3D**) and adjacent to the subducting intrusions within transects 1 and  
 242 4. Positive isopycnal strain values were observed at both edges of the subducting intrusion initially, with a predominant  
 243 concentration of positive values indicating stretching of isopycnal surfaces primarily at the bottom edge as subduction  
 244 progressed (**Fig. 3E**). The current data along transect 2 illustrated a horizontal velocity magnitude exceeding  $60 \text{ cm s}^{-1}$  within  
 245 the interior of the anticyclone, while lower values were observed on its periphery. The subducting intrusion, identified beneath  
 246 the superficial high-velocity patch and within a zone of elevated shear squared (primarily due to a negative vertical gradient  
 247 of the zonal velocity component; **Fig. 3F**), was characterized by a horizontal velocity estimated at approximately  $0.5 \text{ m s}^{-1}$ .  
 248 The mean Richardson number across the transect was calculated to be 0.89, indicating a generally stable water column with  
 249 respect to shear instabilities. However, lower Richardson numbers were observed in the initial zone of the intrusion (between  
 250 km 17 and 29 of the transect; **Fig. 3G**). No significant correlation was found between shear and  $\varepsilon$ , suggesting that stratification  
 251 may suppress shear-driven turbulence and/or that other sources of turbulence could be influencing the study area. The  
 252 subducted water exhibited positive potential vorticity (**Fig. 3H**), revealing unfavourable conditions for the generation of  
 253 symmetric instability.

254 A deepening of the well oxygenated surface layer towards the center of the anticyclone was observed in transects 1  
 255 and 2 (**Supplementary Fig. 3** and **Fig. 3**, respectively). Elevated dissolved oxygen anomaly concentrations ( $>0.5 \text{ mg l}^{-1}$ ) were  
 256 detected inside the subducting intrusion along transect 2 (**Fig. 3I**), with high values deepening from approximately 50 to 120  
 257 m. Similarly, anomalous high chlorophyll-a anomaly values were found near the 30 km of transect 2, with anomaly  
 258 concentrations of up to  $1.4 \text{ mg m}^{-3}$  detected at a depth of 100 m (**Fig. 3J**).

259

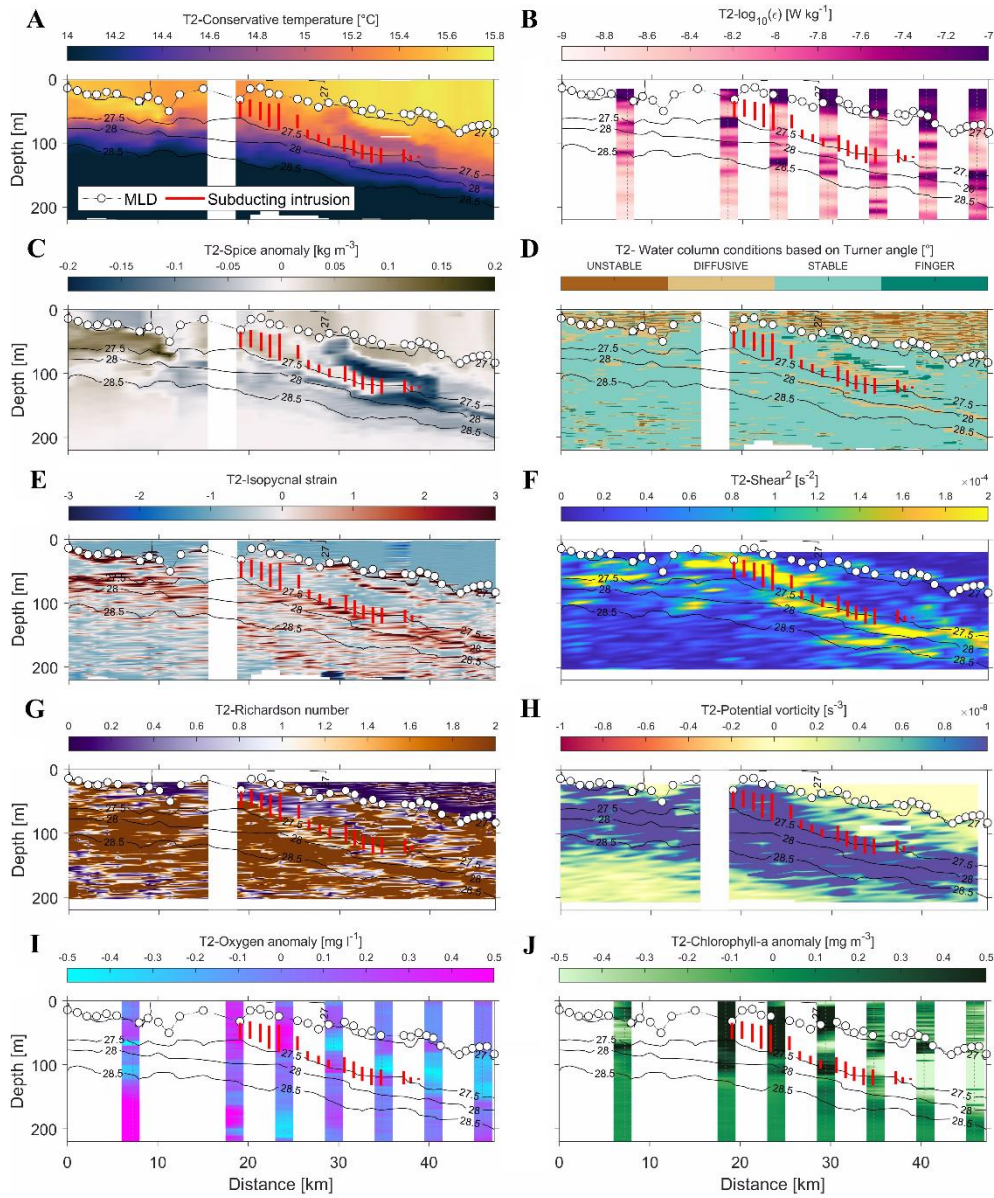


**Figure 3.** Profiles of conservative temperature (A), turbulent kinetic energy dissipation rates (B), spice anomaly (C), water column conditions based on Turner angle estimations (D), isopycnal strain (E), shear squared (F), Richardson number (G), potential vorticity (H), dissolved oxygen anomaly (I), and chlorophyll-a anomaly (J) estimations acquired along transect 2 of the 2019 CALYSPSO campaign. Isopycnals are represented as black lines, while the mixed layer depth and subducting intrusions are denoted by colored points and lines, respectively. The distances between stations were calculated starting from the northernmost sampling point.

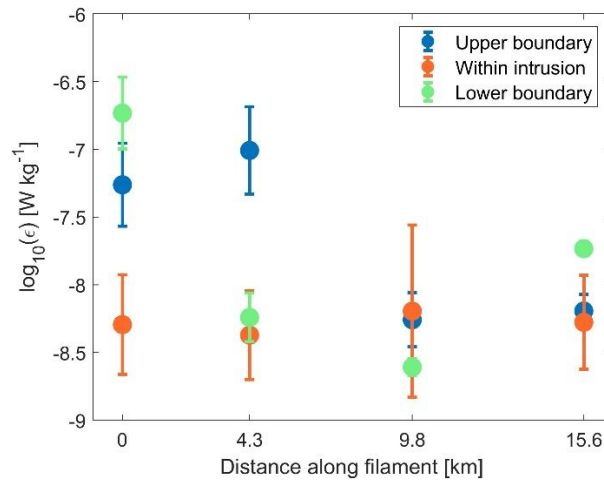
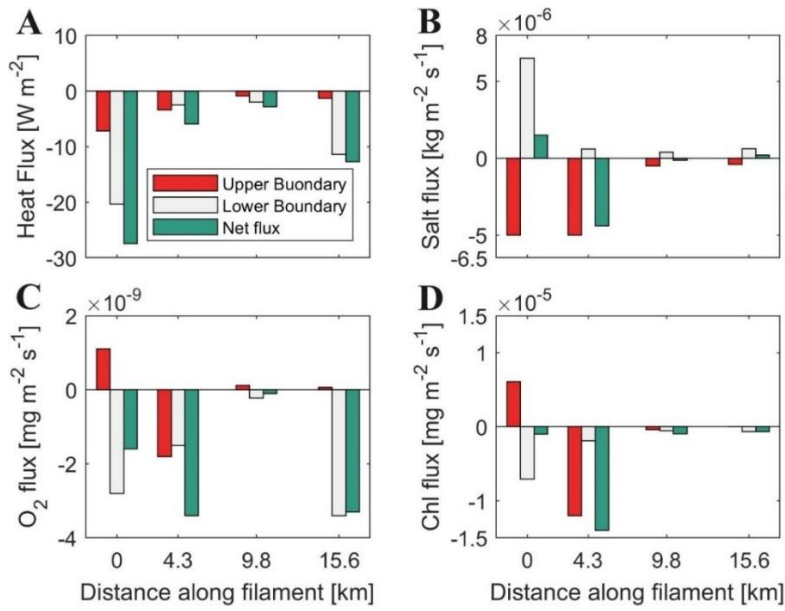


**Figure 4.** Mean turbulent kinetic energy dissipation values within the intrusion and at its upper and lower boundaries (5 m from the intrusion edges). The errorbars represent the measurement standard deviation.

### 3.3 Turbulent fluxes around the subducting intrusion

We focused our analysis of the microstructure profiles to transect 2 during the 2019 CALYPSO campaign due to its higher horizontal resolution (**Fig. 1B**). Turbulent fluxes within the interior of the transect 2 intrusion exhibited reduced values compared to water column around both intrusion edges (**Supplementary Fig. 8**). Notably, turbulent fluxes exhibited higher magnitudes within the first two profiles sampling the edges of the subducting intrusion in comparison to the subsequent two profiles (**Fig. 5**). Turbulent fluxes around the intrusion boundaries resulted in a net loss of heat, oxygen and chlorophyll-a properties from within the intrusion to the surrounding ocean, while salinity increased (**Table 1**). Heat, oxygen and chlorophyll-a turbulent fluxes revealed a consistent properties loss at the base of the intrusion towards the deeper layer, while salt fluxes displayed a coherent property loss (gain) at the upper (lower) boundary of the intrusion. Heat loss was consistently recorded near the upper intrusion boundary at all sampling stations, although more variability was observed in oxygen and chlorophyll-a fluxes. The mean absolute values for turbulent fluxes indicated reduced heat, oxygen and chlorophyll-a fluxes near the upper boundary in contrast to the intrusion's base. Specifically, the upper heat flux accounted for only 35% of the magnitude observed near the base of the intrusion, while the upper oxygen and chlorophyll-a fluxes represented 68 and 63%, respectively, of the corresponding bottom flux magnitudes. The fluxes uncertainty was provided in **Supplementary Table 1**.



285

286 **Figure 5.** Estimations of turbulent fluxes of heat (A), salt (B), oxygen (C) and chlorophyll-a (D) along the upper and lower boundaries of  
 287 the subducting intrusion identified within transect T2 of the 2019 CALYPSO campaign and the resulting net flux (in green). The distances  
 288 between the four stations where the fluxes were calculated (as shown in Supplementary Figure 8) along the subducting intrusion are provided.  
 289 Positive (negative) values for the turbulent fluxes represent a gain (loss) of the respective variables within the interior of the intrusion.

290

291 **Table 1.** Mean ( $\pm$  95% confidence interval) conservative temperature, absolute salinity, dissolved oxygen and chlorophyll-a conditions  
 292 within the subducting intrusion identified along transect T2 and estimations of daily turbulent heat, salt, oxygen and chlorophyll-a fluxes.  
 293 The fluxes were computed as the rate of change of properties  $[(\Delta \text{flux}) (\text{intrusion width})^{-1}]$ . Negative (positive) values denote a loss (gain)  
 294 within the interior of the intrusion. The distances between the four stations, the intrusion mean depth and thickness are provided.

Variable	Distance along transect [km]			
	0	4.3	9.8	15.6
<b>Intrusion characteristics</b>				
Depth [m]	47	59	99	120
Thickness [m]	25.9	42.2	13.3	24.9
<b>Mean properties</b>				
Temperature [ $^{\circ}\text{C}$ ]	$15.28 \pm 0.05$	$15.27 \pm 0.06$	$15.16 \pm 0.03$	$14.91 \pm 0.06$
Salinity [ $\text{g kg}^{-1}$ ]	$37.03 \pm 0.03$	$37.04 \pm 0.04$	$37.10 \pm 0.03$	$37.15 \pm 0.07$
Oxygen [ $\text{mg l}^{-1}$ ]	$7.74 \pm 0.07$	$7.84 \pm 0.10$	$7.43 \pm 0.05$	$7.16 \pm 0.04$
Chlorophyll-a [ $\text{mg m}^{-3}$ ]	$1.81 \pm 0.12$	$2.16 \pm 0.28$	$1.38 \pm 0.13$	$0.68 \pm 0.02$
<b>Daily fluxes</b>				
Heat [ $^{\circ}\text{C d}^{-1}$ ]	$-2.2 \cdot 10^{-2}$	$-2.9 \cdot 10^{-3}$	$-4.4 \cdot 10^{-3}$	$-1.1 \cdot 10^{-2}$
Salt [ $\text{g kg}^{-1} \text{d}^{-1}$ ]	$5.1 \cdot 10^{-3}$	$-9.1 \cdot 10^{-3}$	$-7.6 \cdot 10^{-4}$	$7.0 \cdot 10^{-4}$
Oxygen [ $\text{mg l}^{-1} \text{d}^{-1}$ ]	$-5.5 \cdot 10^{-3}$	$-6.9 \cdot 10^{-3}$	$-6.7 \cdot 10^{-4}$	$-1.1 \cdot 10^{-2}$
Chlorophyll-a [ $\text{mg m}^{-3} \text{d}^{-1}$ ]	$-3.4 \cdot 10^{-3}$	$-2.9 \cdot 10^{-2}$	$-6.2 \cdot 10^{-3}$	$-2.2 \cdot 10^{-3}$

296 **4 Discussion**

297 **4.1 Turbulent kinetic energy dissipation rates in the Western Alboran Sea**

298 The TKE dissipation rates in our study were (mean:  $8.2 \cdot 10^{-9} \text{ W kg}^{-1}$ ) found to be comparable to those reported in previous  
299 investigations involving microstructure data in the Mediterranean Sea. For instance, Cuypers et al. (2012) calculated mean  
300 TKE dissipation values of approximately  $10^{-8} \text{ W kg}^{-1}$  below the seasonal pycnocline. Our TKE dissipation estimates unveiled  
301 an intermediate turbulent environment, between the Mediterranean energetic and quiescent regions (mean:  $5.2 \cdot 10^{-8}$  and  $4.7 \cdot 10^{-10} \text{ W kg}^{-1}$ , respectively; Vladoiu et al., 2021). Interestingly, our findings exhibited a closer resemblance to the TKE dissipation  
302 observed west of the Gibraltar Strait, where the mean TKE dissipation was  $4 \cdot 10^{-9} \text{ W kg}^{-1}$  in the ocean interior (Fernández-  
303 Castro et al., 2014).

305 The observed peaks in TKE dissipation rates were predictably situated in shallow ocean regions influenced by wave  
306 breaking, in close proximity to the base of mixed layer (Zippel et al., 2022) and near the boundaries of subducting intrusions  
307 (**Fig. 3**). However, other peaks were detected at deeper levels and did not appear to correlate with aforementioned factors.  
308 Mixing processes in the stratified ocean below the mixed layer are often attributed to vertical shear extending below the MLD,  
309 penetrative convection and the breaking of internal waves (MacKinnon et al., 2013). The Western Alboran Sea may be  
310 influenced by the eastward propagation of internal waves traveling along isopycnals generated by the interaction of tidal  
311 currents with bathymetry at the Gibraltar Strait (Thorpe, 2007; Alpers et al., 2008; Bolado-Penagos et al., 2023). While  
312 symmetric instabilities have been identified as effective mechanisms for geostrophic energy dissipation in the ocean interior  
313 (Zhou et al., 2022), the positive sign of the potential vorticity associated with subducting water in the study area (**Fig. 3H**)  
314 suggests that the conditions required for this process to occur may not be met. Another plausible explanation for the deep TKE  
315 dissipation peaks could be provided by dissipation associated with subducting intrusions that may have gone undetected by  
316 our methodology. Conducting future surveys with mooring and/or glider deployments to identify internal waves within the  
317 study zone could significantly advance our comprehension of their spatiotemporal variability and their role in generating deep  
318 turbulence along isopycnals.

319 **4.2 Water column regimes**

320 The convergence of Atlantic and Mediterranean waters in the study zone resulted in a robust stratification of the water column,  
321 characterized predominantly by doubly stable conditions. Along isopycnals and at the upper boundary of the subducting  
322 intrusion (**Figure 3**), we observed instances of diffusive convection regimes. While diffusive convection is typically associated  
323 with thermohaline staircases and is more commonly found at higher latitudes (Kelley et al., 2002; van der Boog et al., 2021),  
324 the presence of horizontal variability in temperature and salinity conditions in our study area may lead to the formation of

325 coherent subducting intrusions associated with double diffusive convection (Kelley et al., 2002; Schmitt, 2009). Freilich and  
326 Mahadevan (2021) proposed that the specific pathway of subducting intrusions along isopycnals in the study zone could be  
327 generated by a combination of mesoscale (geostrophic) frontogenesis and submesoscale (ageostrophic) dynamics.

328 The subducting intrusion transports subsurface water column properties into the deeper ocean, undergoing erosion  
329 along its pathway through a combination of turbulent and diffusive mixing. This dynamic process results in a modification of  
330 its inherent properties.

#### 331 **4.3 Turbulent erosion of the intrusion**

332 The elevated TKE dissipation rates in the surface layer, coupled with an increase in stratification with depth can potentially  
333 account for the higher diffusivity and turbulent fluxes observed at the start of the intrusion's subduction compared to stations  
334 sampled further along the subduction path. Moreover, physical and biogeochemical properties of the subducted water  
335 resembled surface conditions more closely than those of the deep layer, resulting in reduced fluxes along the upper boundary  
336 of the intrusion compared to the lower boundary (with the exception of the station located at 4.3 km).

337 The turbulent erosion of the subducting filament led to an overall decrease in temperature, oxygen and chlorophyll-a  
338 content within the filament, while salinity increased (**Table 1**). The slight increment in oxygen and chlorophyll-a concentration  
339 observed at the second station within the intrusion may be attributed to either the properties gain detected at the upper boundary  
340 of the first station, indicating a supply of biogeochemical properties from the surface layer into the intrusion interior, or in situ  
341 phytoplankton production (the photic layer was estimated to be around 60 m deep; **Supplementary Fig. 9**).

342 However, these diapycnal fluxes were too weak to induce a significant dilution of the intrusion, as daily fluxes were  
343 orders of magnitude smaller than the mean property values within the intrusion (**Table 1**). These estimates did not account for  
344 double-diffusive mixing fluxes characteristic of thermohaline staircases, as such features are predominant at greater depths in  
345 the Western Mediterranean Sea (Onken and Brambilla, 2003; Schroeder et al., 2016; Ferron et al., 2021). Despite of this, the  
346 estimates of diffusive convection mixing were negligible compared to the turbulent fluxes. In addition to turbulent and  
347 diffusive convection mixing, the water column density stability and isopycnal mixing might contribute to the typical vertical  
348 variability in subsurface ocean temperature and salinity. Specifically, isopycnal mixing might act an important role in the  
349 observed dilution given its contribution in meso- and submesoscale coherent features (Abernathey et al., 2022). Conversely,  
350 the decline in oxygen and chlorophyll-a content with depth can be attributed to the deepening of the photic layer, distance from  
351 the atmospheric-ocean boundary layer, and processes such as remineralization, respiration, and grazing. The modification of  
352 the typical vertical variability in biogeochemical properties induced by subducting intrusions might have profound impacts on  
353 ecosystem dynamics within the study zone.

#### 354 **4.4 Biogeochemical significance of subducting intrusions**

355 The Atlantic Jet, which enters the Mediterranean through the Strait of Gibraltar, coupled with coastal upwelling events,  
356 transforms our study area into one of the most productive zones in the Mediterranean despite the Mediterranean Sea's well-

known status as an oligotrophic basin (Reale et al., 2020; Sánchez-Garrido and Nadal, 2022). The outer boundary of the WAG has also been identified as a stirring region where properties of the water column are continually exchanged as they are advected towards the center of the anticyclone (Brett et al., 2020; Sala et al., 2022). Subduction of the intrusion may enhance particulate organic carbon export below the mixed layer, reducing its exposure time to remineralization (Freilich et al., 2024). This process contributes to one of the highest export rates observed in the Mediterranean Sea based on sediment trap and particle size distribution profiles data (Ramondenc et al., 2016). Additionally, the mixing associated with subducting intrusions may facilitate the reorganization of phytoplankton communities, traditionally stratified in the photic layer (Mena et al., 2019) and their proliferation. This is especially significant, as nitrates are nearly depleted in the shallow layer north of the WAG (Oguz et al., 2014; Lazzari et al., 2016; García-Martínez et al., 2018). It has been demonstrated that oceanic fronts might act as aggregation areas for planktonic organisms, becoming important foraging areas for higher trophic layers (Acha et al., 2015). Moreover, the transport of chlorophyll-a towards the center of the WAG could lead to an increase in the biomass of diel vertical migrant zooplankton, which tends to be more abundant in the inner part of the gyre compared to its periphery (Yebra et al., 2018).

## 5 Conclusions

The Western Alboran Gyre is a dynamical feature characterized by high spatiotemporal variability arising from the convergence of Mediterranean and Atlantic waters. Indeed, the northern edge of the WAG water column exhibited notable spatial variability in both physical and biogeochemical characteristics. Specifically, the inner part of this gyre featured higher temperature, current velocity, oxygen content and chlorophyll-a concentration compared to its periphery. Moreover, there was an observable deepening of enhanced Brunt–Väisälä frequency and turbulent kinetic energy dissipation rates towards the anticyclone's center.

The investigation of spice anomaly spatial variability allowed the identification of several subducting intrusions occurring beneath the mixed layer depth, extending from the gyre's outer region towards its center. High turbulent kinetic energy dissipation rates were evident at both the upper and lower boundaries of these intrusions, complemented by localized peaks at deeper levels. The specific factors contributing to these heightened dissipation rates at deeper levels remain elusive.

The turbulent fluxes of heat, salt, oxygen and chlorophyll-a along the intrusion boundaries revealed a consistent net loss of physical and biogeochemical properties from within the intrusion to the surrounding ocean. From a biogeochemical perspective, the subduction intrusion holds significance as it has the potential to amplify the export of particulate organic carbon below the mixed layer. Additionally, it may contribute to the enhancement of diel vertical migrant zooplankton biomass and facilitate the proliferation of phytoplankton communities. Notably, mixing due to turbulence or diffusive convection contributed little to the observed variation in temperature, salinity, oxygen or chlorophyll-a within the intrusion interior. Other factors, such as water column density stability, variability of the photic layer depth, and organic matter degradation, likely played a role in these dynamics.

389 While our present study has provided valuable insights into the subduction of intrusions and their turbulent erosion  
390 within the Western Alboran Gyre, significant gaps remain in our understanding of the spatiotemporal variability of subducting  
391 intrusions. Future targeted surveys that specifically address the persistence and extent of these features might improve  
392 quantitative parametrizations of key physical and biogeochemical property subduction. Explorations encompassing a broader  
393 surface of the WAG may reveal asymmetries in intrusion subduction between the WAG's edges and offer an estimate of the  
394 total subduction occurring within the WAG.

395

396 *Funding.* CALYPSO constitutes a Departmental Research Initiative funded by the U.S. Office of Naval Research. GT was  
397 founded by ISMAR-26-2022-VE and ISMAR-18-2023-VE research fellowships. TMSJ was supported by ONR grant N00014-  
398 18-1-2416.

399

400 *Data availability.* Data will be made available on request.

401

402 *Author contributions.* GT: Conceptualization, Methodology, Software, Validation, Formal analysis, Data Curation, Writing -  
403 Original Draft, Writing - Review & Editing, Visualization. MD: Methodology, Software, Data Curation, Writing - Original  
404 Draft, Writing - Review & Editing, Supervision. MF: Resources, Writing - Review & Editing. AM: Resources, Writing -  
405 Review & Editing, Project administration, Funding acquisition. SJ: Resources, Writing - Review & Editing. LP: Resources,  
406 Writing - Review & Editing. FF: Conceptualization, Methodology, Software, Data Curation, Writing - Original Draft, Writing  
407 - Review & Editing, Supervision, Project administration, Funding acquisition.

408

409 *Competing interests.* The authors declare that they have no conflict of interest.

410

411 *Acknowledgements.* We extend our sincere appreciation to the captains and crews of the R/V *Pourquoi Pas?*, as well as the  
412 technical and scientific personnel involved in making measurements and providing support. The authors wish to express their  
413 gratitude to Leo Middleton engaging in insightful conversations that influenced the development of this article. Furthermore,  
414 we would like to acknowledge all the CALYPSO researchers whose constructive comments during CALYPSO's Padua  
415 meeting enriched this study. Finally, we thank the editor and reviewers for their valuable assistance, comments, and  
416 suggestions.

## 417 **References**

418 Abernathy, R., Gnanadesikan, A., Pradal, M. A., and Sundermeyer, M. A.: Isopycnal mixing, in: Ocean Mixing: Drivers,  
419 Mechanisms and Impacts, edited by: Meredith, M., and Naveira Garabato, A., Elsevier, 215–256,  
420 <https://doi.org/10.1016/B978-0-12-821512-8.00016-5>, 2022.



421 Acha, E. M., Piola, A., Iribarne, O., and Mianzan, H (Eds.): Ecological processes at marine fronts: Oases in the ocean,  
 422 Springer, Berlin, Germany, 68 pp., ISBN 978-3-319-15479-4, 2015.

423 Alou-Font, M., Carbonero, A., and Allen, J.: NRV Alliance report on delayed mode calibration of chlorophyll data.  
 424 CALYPSO19 cruise 28-03/10-04/19 V-1.0.0, SOCIB-Biogeochemistry Tech. Rep., 2019.

425 Alpers, W., Brandt, P., and Rubino, A.: Internal waves generated in the Straits of Gibraltar and Messina: Observations from  
 426 space, in: Remote Sensing of the European Seas, Springer Netherlands, 319–330, [https://doi.org/10.1007/978-1-4020-](https://doi.org/10.1007/978-1-4020-6772-3_24)  
 427 [6772-3\\_24](https://doi.org/10.1007/978-1-4020-6772-3_24), 2008.

428 Bachman, S. D., Fox-Kemper, B., Taylor, J. R., and Thomas, L. N.: Parameterization of frontal symmetric instabilities. I:  
 429 Theory for resolved fronts, *Ocean Model.*, 109, 72–95, <https://doi.org/10.1016/j.ocemod.2016.12.003>, 2017.

430 Barral, Q. B., Zakardjian, B., Dumas, F., Garreau, P., Testor, P., and Beuvier, J.: Characterization of fronts in the Western  
 431 Mediterranean with a special focus on the North Balearic Front, *Prog. Oceanogr.*, 197, 102636,  
 432 <https://doi.org/10.1016/j.pocean.2021.102636>, 2021.

433 Belkin, I. M., and Cornillon, P. C.: Fronts in the world ocean’s Large Marine Ecosystems, In: International Council for the  
 434 Exploration of the Sea, Annual Science Conference, Helsinki, Finland. CM 2007/D:21, 33 pp., 2007.

435 Bolado-Penagos, M., Sala, I., Jesús Gomiz-Pascual, J., González, C. J., Izquierdo, A., Álvarez, Ó., Vázquez, Á., Bruno, M.,  
 436 and van Haren, H.: Analysis of internal soliton signals and their eastward propagation in the Alboran Sea: exploring the  
 437 effect of subinertial forcing and fortnightly variability, *Prog. Oceanogr.*, 217, 103077,  
 438 <https://doi.org/10.1016/j.pocean.2023.103077>, 2023.

439 Bonaduce, A., Cipollone, A., Johannessen, J. A., Staneva, J., Raj, R. P., and Aydogdu, A.: Ocean mesoscale variability: a case  
 440 study on the Mediterranean sea from a re-analysis perspective, *Front. Earth Sci.*, 9, 816,  
 441 <https://doi.org/10.3389/feart.2021.724879>, 2021.

442 Brett, G. J., Pratt, L. J., Rypina, I. I., and Sánchez-Garrido, J. C.: The western Alboran gyre: An analysis of its properties and  
 443 its exchange with surrounding water, *J. Phys. Oceanogr.*, 50, 3379–3402, <https://doi.org/10.1175/JPO-D-20-0028.1>, 2020.

444 Canuto, V. M., Cheng, Y., and Howard, A. M.: Vertical diffusivities of active and passive tracers, *Ocean Model.*, 36, 198–  
 445 207, <https://doi.org/10.1016/J.OCEMOD.2010.12.002>, 2011.

446 Capó, E. and McWilliams, J. C.: Coherent lagrangian pathways near an east Alboran front, *J. Geophys. Res. Ocean.*, 127,  
 447 e2021JC018022, <https://doi.org/10.1029/2021JC018022>, 2022.

448 Capó, E., Orfila, A., Mason, E., and Ruiz, S.: Energy conversion routes in the western Mediterranean sea estimated from eddy-  
 449 mean flow interactions, *J. Phys. Oceanogr.*, 49, 247–267, <https://doi.org/10.1175/JPO-D-18-0036.1>, 2019.

450 Carpenter, J. R., Rodrigues, A., Schultze, L. K. P., Merckelbach, L. M., Suzuki, N., Baschek, B., and Umlauf, L.: Shear  
 451 Instability and Turbulence Within a Submesoscale Front Following a Storm, *Geophys. Res. Lett.*, 47, e2020GL090365,  
 452 <https://doi.org/10.1029/2020GL090365>, 2020.

453 Chapman, C. C., Lea, M. A., Meyer, A., Sallée, J. B., and Hindell, M.: Defining Southern Ocean fronts and their influence on  
 454 biological and physical processes in a changing climate, <https://doi.org/10.1038/s41558-020-0705-4>, 24 February 2020.

455 Chen, S., Wells, M. L., Huang, R. X., Xue, H., Xi, J., and Chai, F.: Episodic subduction patches in the western North Pacific  
 456 identified from BGC-Argo float data, *Biogeosciences*, 18, 5539–5554, <https://doi.org/10.5194/bg-18-5539-2021>, 2021.

457 Crowe, M. N., and Taylor, J. R.: The evolution of a front in turbulent thermal wind balance. Part 1. Theory, *J. Fluid Mech.*,  
 458 850, 179–211, <https://doi.org/10.1017/jfm.2018.448>, 2018.

459 Cushman-Roisin, B. and Beckers, J.-M.: *Introduction to Geophysical Fluid Dynamics: Physical and Numerical Aspects*,  
 460 Academic Press, ISBN: 978-0-12-088759-0, 2011.

461 Cutolo, E., Pascual, A., Ruiz, S., Shaun Johnston, T. M., Freilich, M., Mahadevan, A., Shcherbina, A., Poulain, P. M.,  
 462 Ozgokmen, T., Centurioni, L. R., Rudnick, D. L., and D’Asaro, E.: Diagnosing Frontal Dynamics From Observations  
 463 Using a Variational Approach, *J. Geophys. Res. Ocean.*, 127, e2021JC018336, <https://doi.org/10.1029/2021JC018336>,  
 464 2022.

465 Cuypers, Y., Bouruet-Aubertot, P., and Marec, C.: Characterization of turbulence from a fine-scale parameterization and  
 466 microstructure measurements in the Mediterranean Sea during the BOUM experiment, *Biogeosciences*, 9, 3131–3149,  
 467 <https://doi.org/10.5194/bg-9-3131-2012>, 2012.

468 D’asaro, E. A.: Turbulence in the upper-ocean mixed layer, *Ann. Rev. Mar. Sci.*, 6, 101–115, [https://doi.org/10.1146/annurev-](https://doi.org/10.1146/annurev-marine-010213-135138)  
 469 [marine-010213-135138](https://doi.org/10.1146/annurev-marine-010213-135138), 2014.

470 D’Asaro, E., Lee, C., Rainville, L., Harcourt, R., and Thomas, L.: Enhanced turbulence and energy dissipation at ocean fronts,  
 471 *Science*, 332, 318–322, <https://doi.org/10.1126/science.1201515>, 2011.

472 de Boyer Montégut, C., Madec, G., Fischer, A. S., Lazar, A., and Iudicone, D.: Mixed layer depth over the global ocean: An  
 473 examination of profile data and a profile-based climatology, *J. Geophys. Res. Ocean.*, 109, 1–20,  
 474 <https://doi.org/10.1029/2004JC002378>, 2004.

475 Dever, M., Freilich, M., Hodges, B., Farrar, J., Lanagan, T., and Mahadevan, A.: UCTD and ECOCTD observations from the  
 476 CALYPSO pilot experiment (2018): Cruise and data report. Woods Hole Oceanographic Institution Tech. Rep., WHOI-  
 477 2019-01, <https://doi.org/10.1575/1912/23637>, 2019.

478 Du, C., Liu, Z., Kao, S. J., and Dai, M.: Diapycnal Fluxes of Nutrients in an Oligotrophic Oceanic Regime: The South China  
 479 Sea, *Geophys. Res. Lett.*, 44, 11, 510–11, 518, <https://doi.org/10.1002/2017GL074921>, 2017.

480 Fedele, G., Mauri, E., Notarstefano, G., and Poulain, P. M.: Characterization of the Atlantic Water and Levantine Intermediate  
 481 Water in the Mediterranean Sea using 20 years of Argo data, *Ocean Sci.*, 18, 129–142, [https://doi.org/10.5194/os-18-129-](https://doi.org/10.5194/os-18-129-2022)  
 482 [2022](https://doi.org/10.5194/os-18-129-2022), 2022.

483 Fer, I., Dengler, M., Holtermann, P., Le Boyer, A., and Lueck, R.: ATOMIX benchmark datasets for dissipation rate  
 484 measurements using shear probes, *Sci. Data*, 11, 518, <https://doi.org/10.1038/s41597-024-03323-y>, 2024.

485 Fernández-Castro, B., Mouriño-Carballido, B., Benítez-Barrios, V. M., Chouciño, P., Fraile-Nuez, E., Graña, R., Piedeleu, M.,  
 486 and Rodríguez-Santana, A.: Microstructure turbulence and diffusivity parameterization in the tropical and subtropical  
 487 Atlantic, Pacific and Indian Oceans during the Malaspina 2010 expedition, *Deep. Res. Part I Oceanogr. Res. Pap.*, 94, 15–  
 488 30, <https://doi.org/10.1016/j.dsr.2014.08.006>, 2014.

489 Ferron, B., Bouruet-Aubertot, P., Schroeder, K., Bryden, H. L., Cuypers, Y., and Borghini, M.: Contribution of Thermohaline  
 490 Staircases to Deep Water Mass Modifications in the Western Mediterranean Sea From Microstructure Observations, *Front.*  
 491 *Mar. Sci.*, 8, 544, <https://doi.org/10.3389/fmars.2021.664509>, 2021.

492 Forryan, A., Allen, J. T., Edhouse, E., Silburn, B., Reeve, K., and Tesi, E.: Turbulent mixing in the eddy transport of Western  
 493 Mediterranean Intermediate Water to the Alboran Sea, *J. Geophys. Res. Ocean.*, 117, 9008,  
 494 <https://doi.org/10.1029/2012JC008284>, 2012.

495 Freilich, M. A., Poirier, C., Dever, M., Alou-Font, E., Allen, J., Cabornero, A., Sudek, L., Choi, C. J., Ruiz, S., Pascual, A.,  
 496 Farrar, J. T., Johnston, T. M. S., D'Asaro, E., Worden, A. Z., and Mahadevan, A.: 3D-intrusions transport active surface  
 497 microbial assemblages to the dark ocean, *bioRxiv*, 121, 2023.09.14.557835, <https://doi.org/10.1073/PNAS.2319937121>,  
 498 2023.

499 Freilich, M. and Mahadevan, A.: Coherent Pathways for Subduction From the Surface Mixed Layer at Ocean Fronts, *J.*  
 500 *Geophys. Res. Ocean.*, 126, e2020JC017042, <https://doi.org/10.1029/2020JC017042>, 2021.

501 Garcia-Jove, M., Mourre, B., Zarokanellos, N. D., Lermusiaux, P. F. J., Rudnick, D. L., and Tintoré, J.: Frontal Dynamics in  
 502 the Alboran Sea: 2. Processes for Vertical Velocities Development, *J. Geophys. Res. Ocean.*, 127, e2021JC017428,  
 503 <https://doi.org/10.1029/2021JC017428>, 2022.

504 García-Martínez, M. del C., Vargas-Yáñez, M., Moya, F., Santiago, R., Muñoz, M., Reul, A., Ramírez, T., and Balbín, R.:  
 505 Average nutrient and chlorophyll distributions in the western Mediterranean: RADMED project, *Oceanologia*, 61, 143–  
 506 169, <https://doi.org/10.1016/j.oceano.2018.08.003>, 2019.

507 Gregg, M. C.: Scaling turbulent dissipation in the thermocline, *J. Geophys. Res. Ocean.*, 94, 9686–9698,  
 508 <https://doi.org/10.1029/jc094ic07p09686>, 1989.

509 Gregg, M. C., D'Asaro, E. A., Riley, J. J., and Kunze, E.: Mixing efficiency in the ocean, *Ann. Rev. Mar. Sci.*, 10, 443–473,  
 510 <https://doi.org/10.1146/annurev-marine-121916-063643>, 2018.

511 IOC, SCOR, and IAPSO: The international thermodynamic equation of seawater – 2010: Calculation and use of  
 512 thermodynamic properties. Intergovernmental Oceanographic Commission, Manuals and Guides, 56, UNESCO, 196 pp.,  
 513 2010.

514 Johnson, A. R. and Omand, M. M.: Evolution of a Subducted Carbon-Rich Filament on the Edge of the North Atlantic Gyre,  
 515 *J. Geophys. Res. Ocean.*, 126, e2020JC016685, <https://doi.org/10.1029/2020JC016685>, 2021.

516 Johnston, T. M. S., Rudnick, D. L., and Pallàs-Sanz, E.: Elevated mixing at a front, *J. Geophys. Res. Ocean.*, 116, 11033,  
 517 <https://doi.org/10.1029/2011JC007192>, 2011.

518 Kelley, D. E., Fernando, H. J. S., Gargett, A. E., Tanny, J., and Özsoy, E.: The diffusive regime of double-diffusive convection,  
 519 *Prog. Oceanogr.*, 56, 461–481, [https://doi.org/10.1016/S0079-6611\(03\)00026-0](https://doi.org/10.1016/S0079-6611(03)00026-0), 2003.

520 Klein, P. and Lapeyre, G.: The oceanic vertical pump induced by mesoscale and submesoscale turbulence, *Ann. Rev. Mar.*  
 521 *Sci.*, 1, 351–375, <https://doi.org/10.1146/annurev.marine.010908.163704>, 2009.

522 Lazzari, P., Solidoro, C., Salon, S., and Bolzon, G.: Spatial variability of phosphate and nitrate in the Mediterranean Sea: A  
523 modeling approach, *Deep. Res. Part I Oceanogr. Res. Pap.*, 108, 39–52, <https://doi.org/10.1016/j.dsr.2015.12.006>, 2016.

524 Le Boyer, A., Couto, N., Alford, M. H., Drake, H. F., Bluteau, C. E., Hughes, K. G., Naveira Garabato, A. C., Moulin, A. J.,  
525 Peacock, T., Fine, E. C., Mashayek, A., Cimoli, L., Meredith, M. P., Melet, A., Fer, I., Dengler, M., and Stevens, C. L.:  
526 Turbulent diapycnal fluxes as a pilot Essential Ocean Variable, *Front. Mar. Sci.*, 10, 1241023,  
527 <https://doi.org/10.3389/fmars.2023.1241023>, 2023.

528 Llorc, J., Langlais, C., Matear, R., Moreau, S., Lenton, A., and Strutton, P. G.: Evaluating Southern Ocean Carbon Eddy-Pump  
529 From Biogeochemical-Argo Floats, *J. Geophys. Res. Ocean.*, 123, 971–984, <https://doi.org/10.1002/2017JC012861>, 2018.

530 Lozovatsky, I. D., Fernando, H. J. S., Jinadasa, S. U. P., and Wijesekera, H. W.: Eddy diffusivity in stratified ocean: a case  
531 study in Bay of Bengal, *Environ. Fluid Mech.*, 1–13, <https://doi.org/10.1007/s10652-022-09872-3>, 2022.

532 Lueck, R., Fer, I., Bluteau, C., Dengler, M., Holtermann, P., Inoue, R., LeBoyer, A., Nicholson, S. A., Schulz, K., and Stevens,  
533 C.: Best practices recommendations for estimating dissipation rates from shear probes, *Front. Mar. Sci.*, 11, 1334327,  
534 <https://doi.org/10.3389/fmars.2024.1334327>, 2024.

535 MacKinnon, J., St Laurent, L., and Naveira Garabato, A. C.: Diapycnal mixing processes in the ocean interior, in: *International*  
536 *Geophysics*, vol. 103, Academic Press, 159–183, <https://doi.org/10.1016/B978-0-12-391851-2.00007-6>, 2013.

537 Mahadevan, A.: The Impact of Submesoscale Physics on Primary Productivity of Plankton, *Ann. Rev. Mar. Sci.*, 8, 161–184,  
538 <https://doi.org/10.1146/annurev-marine-010814-015912>, 2016.

539 Mahadevan, A., Pascual, A., Rudnick, D. L., Ruiz, S., Tintoré, J., and D’Asaro, E.: Coherent pathways for vertical transport  
540 from the surface ocean to interior, *Bull. Am. Meteorol. Soc.*, 101, E1996–E2004, <https://doi.org/10.1175/BAMS-D-19->  
541 0305.1, 2020a.

542 Mahadevan, A., D’Asaro, E. A., Allen, J. T., Almaraz García, P., Alou-Font, E., Aravind, H. M., Balaguer, P., Caballero, I.,  
543 Calafat, N., Carbornero, A., Casas, B., Castilla, C., Centurioni, L. R., Conley, M., Cristofano, G., Cutolo, E., Dever, M.,  
544 Enrique Navarro, A., Falcieri, F., Freilich, M., Goodwin, E., Graham, R., Guigand, C., Hodges, B. A., Huntley, H.,  
545 Johnston, S., Lankhorst, M., Lermusiaux, P. F. J., Lizaran, I., Mirabito, C., Miralles, A., Mourre, B., Navarro, G., Ohmart,  
546 M., Ouala, S., Ozgokmen, T. M., Pascual, A., Pou, J. M. H., Poulain, P. M., Ren, A., Rodriguez Tarry, D., Rudnick, D. L.,  
547 Rubio, M., Ruiz, S., Rypina, I. I., Tintore, J., Send, U., Shcherbina, A. Y., Torner, M., Salvador-Vieira, G., Wirth, N., and  
548 Zarokanellos, N.: CALYPSO 2019 Cruise Report: field campaign in the Mediterranean, Woods Hole Oceanographic  
549 Institution, <https://doi.org/10.1575/1912/25266>, 2020b.

550 McDougall, T. J., Thorpe, S. A., and Gibson, C. H.: Small-Scale Turbulence and Mixing in the Ocean: A Glossary, in: *Small-*  
551 *scale turbulence and mixing in the ocean*, vol. 46, edited by: Nihoul, J. C. J. and Jamart, B. M., Elsevier, 3–9,  
552 [https://doi.org/10.1016/S0422-9894\(08\)70533-6](https://doi.org/10.1016/S0422-9894(08)70533-6), 1988.

553 McDougall, T. and Krzysik, O.: Spiciness, *J. Mar. Res.*, 73, 141–152, <https://doi.org/10.1357/002224015816665589>, 2015

554 McDougall, T. J., Barker, P. M., and Stanley, G. J.: Spice Variables and Their Use in Physical Oceanography, *J. Geophys.*  
555 *Res. Ocean.*, 126, e2019JC01593, <https://doi.org/10.1029/2019JC015936>, 2021.

556 McWilliams, J. C.: Oceanic Frontogenesis, *Ann. Rev. Mar. Sci.*, 13, 227–253, [https://doi.org/10.1146/annurev-marine-](https://doi.org/10.1146/annurev-marine-032320-120725)  
557 032320-120725, 2021.

558 Mena, C., Reglero, P., Hidalgo, M., Sintes, E., Santiago, R., Martín, M., Moyà, G., and Balbín, R.: Phytoplankton community  
559 structure is driven by stratification in the oligotrophic mediterranean sea, *Front. Microbiol.*, 10, 456694,  
560 <https://doi.org/10.3389/fmicb.2019.01698>, 2019.

561 Mouriño-Carballido, B., Otero Ferrer, J. L., Fernández Castro, B., Marañón, E., Blazquez Maseda, M., Aguiar-González, B.,  
562 Chouciño, P., Graña, R., Moreira-Coello, V., and Villamaña, M.: Magnitude of nitrate turbulent diffusion in contrasting  
563 marine environments, *Sci. Rep.*, 11, 1–16, <https://doi.org/10.1038/s41598-021-97731-4>, 2021.

564 Nasmyth, P. W.: Oceanic turbulence, Ph.D. thesis, University of British Columbia, Canada,  
565 <https://doi.org/10.14288/1.0302459>, 1970.

566 Oguz, T., Macias, D., Garcia-Lafuente, J., Pascual, A., and Tintore, J.: Fueling plankton production by a meandering frontal  
567 jet: A case study for the Alboran sea (Western Mediterranean), *PLoS One*, 9, e111482,  
568 <https://doi.org/10.1371/journal.pone.0111482>, 2014.

569 Olita, A., Capet, A., Claret, M., Mahadevan, A., Poulain, P. M., Ribotti, A., Ruiz, S., Tintoré, J., Tovar-Sánchez, A., and  
570 Pascual, A.: Frontal dynamics boost primary production in the summer stratified Mediterranean sea, *Ocean Dyn.*, 67, 767–  
571 782, <https://doi.org/10.1007/s10236-017-1058-z>, 2017.

572 Omand, M. M., D’Asaro, E. A., Lee, C. M., Perry, M. J., Briggs, N., Cetinić, I., and Mahadevan, A.: Eddy-driven subduction  
573 exports particulate organic carbon from the spring bloom, *Science*, 348, 222–225, <https://doi.org/10.1126/science.1260062>,  
574 2015.

575 Onken, R. and Brambilla, E.: Double diffusion in the Mediterranean Sea: Observation and parameterization of salt finger  
576 convection, *J. Geophys. Res. Ocean.*, 108, 8124, <https://doi.org/10.1029/2002jc001349>, 2003.

577 Pinkel, R., Sherman, J., Smith, J., and Anderson, S.: Strain: Observations of the Vertical Gradient of Isopycnal Vertical  
578 Displacement, *J. Phys. Oceanogr.*, 21, 527–540, [https://doi.org/10.1175/1520-0485\(1991\)021<0527:sootvg>2.0.co;2](https://doi.org/10.1175/1520-0485(1991)021<0527:sootvg>2.0.co;2),  
579 1991.

580 Ramondenc, S., Madeleine, G., Lombard, F., Santinelli, C., Stemmann, L., Gorsky, G., and Guidi, L.: An initial carbon export  
581 assessment in the Mediterranean Sea based on drifting sediment traps and the Underwater Vision Profiler data sets, *Deep.*  
582 *Res. Part I Oceanogr. Res. Pap.*, 117, 107–119, <https://doi.org/10.1016/j.dsr.2016.08.015>, 2016.

583 Reale, M., Giorgi, F., Solidoro, C., Di Biagio, V., Di Sante, F., Mariotti, L., Farneti, R., and Sannino, G.: The Regional Earth  
584 System Model RegCM-ES: Evaluation of the Mediterranean Climate and Marine Biogeochemistry, *J. Adv. Model. Earth*  
585 *Syst.*, 12, e2019MS001812, <https://doi.org/10.1029/2019MS001812>, 2020.

586 Rudnick, D. L. and Klinke, J.: The underway conductivity-temperature-depth instrument, *J. Atmos. Ocean. Technol.*, 24,  
587 1910–1923, <https://doi.org/10.1175/JTECH2100.1>, 2007.

588 Rudnick, D. L., Zarokanellos, N. D., and Tint, J.: A Four-Dimensional Survey of the Almeria–Oran Front by Underwater  
589 Gliders: Tracers and Circulation, *J. Phys. Oceanogr.*, 52, 225–242, <https://doi.org/10.1175/JPO-D-21-0181.1>, 2022.

590 Ruiz, S., Claret, M., Pascual, A., Olita, A., Troupin, C., Capet, A., Tovar-Sánchez, A., Allen, J., Poulain, P. M., Tintoré, J.,  
591 and Mahadevan, A.: Effects of Oceanic Mesoscale and Submesoscale Frontal Processes on the Vertical Transport of  
592 Phytoplankton, *J. Geophys. Res. Ocean.*, 124, 5999–6014, <https://doi.org/10.1029/2019JC015034>, 2019.

593 Sala, I., Bolado-Penagos, M., Bartual, A., Bruno, M., García, C. M., López-Urrutia, Á., González-García, C., and Echevarría,  
594 F.: A Lagrangian approach to the Atlantic Jet entering the Mediterranean Sea: Physical and biogeochemical  
595 characterization, *J. Mar. Syst.*, 226, 103652, <https://doi.org/10.1016/j.jmarsys.2021.103652>, 2022.

596 Sánchez-Garrido, J. C. and Nadal, I.: The Alboran Sea circulation and its biological response: A review, *Front. Mar. Sci.*, 9,  
597 933390, <https://doi.org/10.3389/fmars.2022.933390>, 2022.

598 Schmitt, R. W.: Double-Diffusive Convection, in: *Encyclopedia of Ocean Sciences*, Academic Press, 162–170,  
599 <https://doi.org/10.1016/B978-012374473-9.00604-4>, 2009.

600 Schroeder, K., Chiggiato, J., Bryden, H. L., Borghini, M., and Ben Ismail, S.: Abrupt climate shift in the Western  
601 Mediterranean Sea, *Sci. Rep.*, 6, 1–7, <https://doi.org/10.1038/srep23009>, 2016.

602 Schulz, K., Mohrholz, V., Fer, I., Janout, M., Hoppmann, M., Schaffer, J., and Koenig, Z.: A full year of turbulence  
603 measurements from a drift campaign in the Arctic Ocean 2019–2020, *Sci. Data*, 9, 1–11, [https://doi.org/10.1038/s41597-](https://doi.org/10.1038/s41597-022-01574-1)  
604 022-01574-1, 2022.

605 Sheehan, P. M. F., Damerell, G. M., Leadbitter, P. J., Heywood, K. J., and Hall, R. A.: Turbulent kinetic energy dissipation  
606 rate and associated fluxes in the western tropical Atlantic estimated from ocean glider observations, *Ocean Sci.*, 19, 77–  
607 92, <https://doi.org/10.5194/os-19-77-2023>, 2023.

608 Shroyer, E. L., Nash, J. D., Waterhouse, A. F., and Moum, J. N.: Measuring Ocean Turbulence, in: *Observing the Oceans in*  
609 *Real Time*, edited by: Venkatesan, R., Tandon, A., D’Asaro, E., and Atmanand, M. A., Springer, Cham, 99–122,  
610 [https://doi.org/10.1007/978-3-319-66493-4\\_6](https://doi.org/10.1007/978-3-319-66493-4_6), 2018.

611 Storer, B. A., Buzzicotti, M., Khatri, H., Griffies, S. M., and Aluie, H.: Global energy spectrum of the general oceanic  
612 circulation, *Nat. Commun.*, 13, 1–9, <https://doi.org/10.1038/s41467-022-33031-3>, 2022.

613 Stukel, M. R., Aluwihare, L. I., Barbeau, K. A., Chekalyuk, A. M., Goericke, R., Miller, A. J., Ohman, M. D., Ruacho, A.,  
614 Song, H., Stephens, B. M., and Landry, M. R.: Mesoscale ocean fronts enhance carbon export due to gravitational sinking  
615 and subduction, *Proc. Natl. Acad. Sci. U. S. A.*, 114, 1252–1257, <https://doi.org/10.1073/pnas.1609435114>, 2017.

616 Sudre, F., Hernández-Carrasco, I., Mazoyer, C., Sudre, J., Dewitte, B., Garçon, V., and Rossi, V.: An ocean front dataset for  
617 the Mediterranean sea and southwest Indian ocean, *Sci. Data*, 10, 1–15, <https://doi.org/10.1038/s41597-023-02615-z>, 2023.

618 Tanhua, T., Hainbucher, D., Schroeder, K., Cardin, V., Álvarez, M., and Civitarese, G.: The Mediterranean Sea system: A  
619 review and an introduction to the special issue, *Ocean Sci.*, 9, 789–803, <https://doi.org/10.5194/os-9-789-2013>, 2013.

620 Taylor, G. I.: Statistical theory of turbulence, *Proc. R. Soc. London. Ser. A - Math. Phys. Sci.*, 151, 421–444,  
621 <https://doi.org/10.1098/rspa.1935.0158>, 1935.

622 Thomas, L. N., Taylor, J. R., Ferrari, R., and Joyce, T. M.: Symmetric instability in the Gulf Stream, *Deep. Res. Part II Top.*  
623 *Stud. Oceanogr.*, 91, 96–110, <https://doi.org/10.1016/j.dsr2.2013.02.025>, 2013.

624 Thorpe, S. A.: An introduction to ocean turbulence, Cambridge University Press, England, 291 pp.,  
625 <https://doi.org/10.1017/CBO9780511801198>, 2007.

626 Thorpe, S. A.: The turbulent ocean, Cambridge University Press, England, 439 pp.,  
627 <https://doi.org/10.1017/CBO9780511819933>, 2005.

628 van der Boog, C. G., Dijkstra, H. A., Pietrzak, J. D., and Katsman, C. A.: Double-diffusive mixing makes a small contribution  
629 to the global ocean circulation, *Commun. Earth Environ.*, 2, 1–9, <https://doi.org/10.1038/s43247-021-00113-x>, 2021.

630 van Haren, H.: Sensitive Temperature Probes Detail Different Turbulence Processes in the Deep Mediterranean,  
631 *Oceanography*, 36, <https://doi.org/10.5670/OCEANOGRAPHY.2023.108>, 2023.

632 van Haren, H., Millot, C., and Taupier-Letage, I.: Fast deep sinking in Mediterranean eddies, *Geophys. Res. Lett.*, 33, 4606,  
633 <https://doi.org/10.1029/2005GL025367>, 2006.

634 Vladioiu, A., Bouruet-Aubertot, P., Cuypers, Y., Ferron, B., Schroeder, K., Borghini, M., and Leizour, S.: Contrasted mixing  
635 efficiency in energetic versus quiescent regions: Insights from microstructure measurements in the Western Mediterranean  
636 Sea, *Prog. Oceanogr.*, 195, 102594, <https://doi.org/10.1016/j.pocean.2021.102594>, 2021.

637 Williams, C., Sharples, J., Green, M., Mahaffey, C., and Rippeth, T.: The maintenance of the subsurface chlorophyll maximum  
638 in the stratified western Irish Sea, *Limnol. Oceanogr. Fluids Environ.*, 3, 61–73, <https://doi.org/10.1215/21573689-2285100>, 2013.

640 Williams, R. G.: Ocean Subduction, in: *Encyclopedia of Ocean Sciences: Second Edition*, Academic Press, 156–166,  
641 <https://doi.org/10.1016/B978-012374473-9.00109-0>, 2001.

642 Yebra, L., Herrera, I., Mercado, J. M., Cortés, D., Gómez-Jakobsen, F., Alonso, A., Sánchez, A., Salles, S., and Valcárcel-  
643 Pérez, N.: Zooplankton production and carbon export flux in the western Alboran Sea gyre (SW Mediterranean), *Prog.*  
644 *Oceanogr.*, 167, 64–77, <https://doi.org/10.1016/j.pocean.2018.07.009>, 2018.

645 Zarokanellos, N. D., Rudnick, D. L., Garcia-Jove, M., Mourre, B., Ruiz, S., Pascual, A., and Tintoré, J.: Frontal Dynamics in  
646 the Alboran Sea: 1. Coherent 3D Pathways at the Almeria-Oran Front Using Underwater Glider Observations, *J. Geophys.*  
647 *Res. Ocean.*, 127, e2021JC017405, <https://doi.org/10.1029/2021JC017405>, 2022.

648 Zhmur, V. V., Novoselova, E. V., and Belonenko, T. V.: Potential Vorticity in the Ocean: Ertel and Rossby Approaches with  
649 Estimates for the Lofoten Vortex, *Izv. - Atmos. Ocean Phys.*, 57, 632–641, <https://doi.org/10.1134/S0001433821050157>,  
650 2021.

651 Zhou, H., Dewar, W., Yang, W., Liu, H., Chen, X., Li, R., Liu, C., and Gopalakrishnan, G.: Observations and modeling of  
652 symmetric instability in the ocean interior in the Northwestern Equatorial Pacific, *Commun. Earth Environ.*, 3, 1–11,  
653 <https://doi.org/10.1038/s43247-022-00362-4>, 2022.

654 Zippel, S. F., Farrar, J. T., Zappa, C. J., and Plueddemann, A. J.: Parsing the Kinetic Energy Budget of the Ocean Surface  
655 Mixed Layer, <https://doi.org/10.1029/2021GL095920>, 28 January 2022.

656